APPLIED PHYSICS

Metal oxide semiconductor nanomembrane–based soft unnoticeable multifunctional electronics for wearable human-machine interfaces

Kyoseung Sim[1], Zhoulyu Rao[1], Zhanan Zou[2], Faheem Ershad[3], Jianming Lei[4], Anish Thukral[4], Jie Chen[4,5], Qing-An Huang[5], Jianliang Xiao[2], Cunjiang Yu[1,3,4,6]*

Wearable human-machine interfaces (HMIs) are an important class of devices that enable human and machine interaction and teaming. Recent advances in electronics, materials, and mechanical designs have offered avenues toward wearable HMI devices. However, existing wearable HMI devices are uncomfortable to use and restrict the human body's motion, show slow response times, or are challenging to realize with multiple functions. Here, we report sol-gel-on-polymer–processed indium zinc oxide semiconductor nanomembrane–based ultrathin stretchable electronics with advantages of multifunctionality, simple manufacturing, imperceptible wearing, and robust interfacing. Multifunctional wearable HMI devices range from resistive random-access memory for data storage to field-effect transistors for interfacing and switching circuits, to various sensors for health and body motion sensing, and to microheaters for temperature delivery. The HMI devices can be not only seamlessly worn by humans but also implemented as prosthetic skin for robotics, which offer intelligent feedback, resulting in a closed-loop HMI system.

INTRODUCTION

Wearable human-machine interfaces (HMIs) function as direct communication pathways between humans and machines (1). They primarily sense physical and/or electrophysiological parameters from the wearers and then enable the machines to perform specific functions correspondingly. Recent developments in electronics, materials, and mechanical designs offer avenues toward wearable HMI devices. One avenue involves interconnecting and packaging commercially available rigid electronic chips and sensors in an appropriate format to enable the desired electrical and sensing functions. However, these wearable HMIs are mostly semisoft (2, 3); therefore, they are uncomfortable to use, restrict the human body's motion, and/or cannot adapt to the deformations from the human body's dynamic range of motion (4, 5). Soft elastic electronic materials that perfectly meet the requirements of deformability and stretchability offer an alternative to constructing the stretchable wearable HMI devices (4, 6). For instance, soft rubbery materials–based sensory systems with resistive sensing characteristics have been widely used for wearable sensing systems (7, 8). However, these rubbery materials feature slow response times and undergo substantial hysteresis upon cyclic deformations (8, 9). Inorganic materials, however, exhibit fast response times and negligible hysteresis and therefore have been adopted for wearable electronics and sensors (10–12). Owing to nonstretchable mechanical characteristics of these inorganic materials, mechanical structures such as wrinkling, serpentine, and kirigami (10, 13–15) serve as key enablers for wearable HMI devices with soft stretchable characteristics. Although the last two approaches based on

elastic materials and structural designs for wearable HMI devices have certain advantages in mechanical softness, they face technical challenges, especially to achieve multiple functions. For instance, to achieve multiple functions, such as sensing, switching, stimulation, and data storage, many different types of electronic functional materials are needed and heterogeneous integration technologies such as transfer printing are used (10, 14). These devices are usually associated with complex fabrication, process incompatibility, low scalability, and high cost. In addition, the teaming between human and machines is closer, where interaction, understanding, and communication among each other are expected (16–19). As a result, wearable HMI devices are needed not only for humans but also for machines to form closed-loop pathways. Therefore, efforts are still needed to develop wearable HMI devices to close the existing technology gaps.

Here, we report an ultrathin, mechanically imperceptible, and stretchable HMI device, which is worn on human skin to capture multiple physical data and also on a robot to offer intelligent feedback, forming a closed-loop HMI. The multifunctional soft stretchable HMI device is based on a one-step formed, sol-gel-on-polymer–processed indium zinc oxide (IZO) semiconductor nanomembrane electronics. Stretchable resistive random-access memory (ReRAM) for data storage components as well as field-effect transistors (FETs) for interfacing and switching circuits, temperature, strain, and ultraviolet (UV) sensors are developed. The devices are made simultaneously without the need for combining multiple functional materials, devices, and excessive heterogeneous integration steps. The devices are constructed in an ultrathin (3 to 4 μm) and narrow meandering serpentine-shaped open-mesh configuration, which renders their mechanical stretchability (stable operation up to 30%). This allows the user to be unaware of the device while it extracts useful signals. We illustrated the multifunctionality of the IZO nanomembrane–based closed-loop HMIs, where the wearable device collects signals from the human muscle, directly guides the robot, and allows the user to feel what the robotic hand experiences. The collective studies on the materials and device design, fabrication, and characterization

[1]Materials Science and Engineering Program, University of Houston, Houston, TX 77204, USA. [2]Department of Mechanical Engineering, University of Colorado, Boulder, CO 80309, USA. [3]Department of Biomedical Engineering, University of Houston, Houston, TX 77204, USA. [4]Department of Mechanical Engineering, University of Houston, Houston, TX 77204, USA. [5]Key Laboratory of MEMS of the Ministry of Education, Southeast University, Nanjing, Jiangsu 210096, China. [6]Department of Electrical and Computer Engineering and Texas Center for Superconductivity, University of Houston, Houston, TX 77204, USA.
*Corresponding author. Email: cyu13@central.uh.edu

demonstrate the fundamental aspects and applicability of these metal oxide nanomembrane–based multifunctional HMI devices.

RESULTS

Ultrathin, mechanically imperceptible, multifunctional HMI device

Figure 1A shows the schematic illustration of an exploded view of the ultrathin, mechanically imperceptible, multifunctional HMI device. Specifically, the HMI device is composed of an IZO nanomembrane–

based ReRAM array, FET array, distributed temperature sensors, UV sensors, strain sensors, and Au-based thermal stimulators (fig. S1A). All devices were fabricated concurrently on a thin (~2 μm) polyimide (PI) layer by spin coating on top of a rigid glass holding substrate, which allows easy release of the devices to become free-standing as described here. The Au electrode, designed in a serpentine configuration to ensure stretchability, was formed with conventional e-beam evaporation, photolithography, and wet etching. The IZO precursor solution [3 mM $Zn(OAc)_2 \cdot 2H_2O$ and 3.5 mM $In(NO_3)_3 \cdot 4H_2O$ in 2-methoxyethanol] was then spin-coated, followed by annealing,
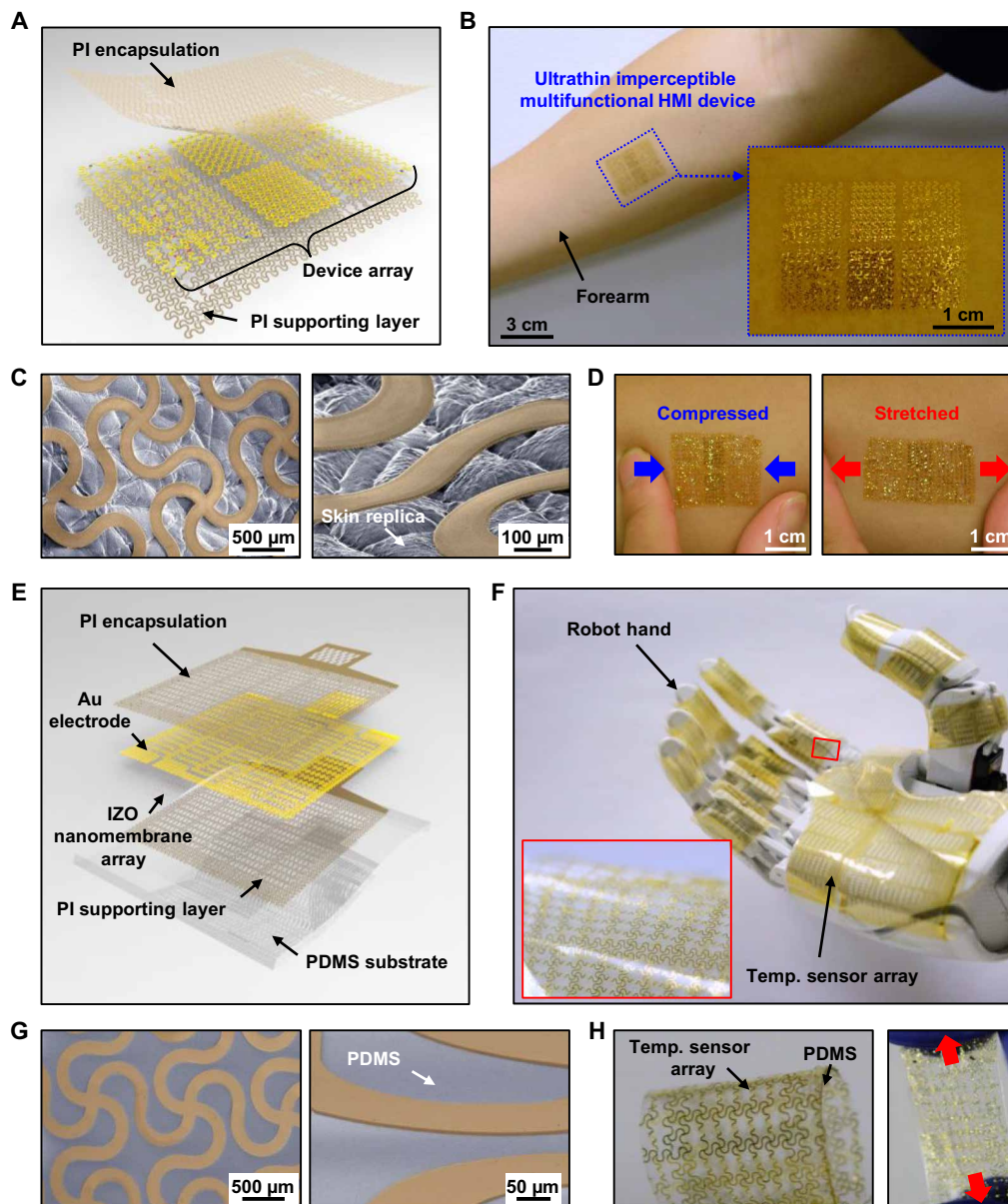
Fig. 1. Ultrathin, stretchable, mechanically imperceptible, multifunctional HMI device for human and robotics. (**A**) Schematic exploded view of an ultrathin multifunctional HMI device. (**B**) Optical image of the device on a human forearm. Inset is a magnified image. (**C**) SEM image of the device on a piece of replicated skin. (**D**) Optical images of the device on a human skin under mechanical deformation: compressed (left) and stretched (right). (**E**) Schematic exploded view of the temperature sensor array for the robotic hand. (**F**) Optical image of the temperature sensor array on a robotic hand. Inset is a magnified image. (**G**) SEM images of the temperature sensor array. (**H**) Optical images of the temperature sensor array on the robotic hand under mechanical deformation: bent (left) and stretched (right). Photo credit: Kyoseung Sim, University of Houston.

photolithography, and wet etching, to define the planar geometries of the ~50-nm-thick IZO nanomembrane pattern for all the functional devices. Another Au electrode was deposited and patterned by liftoff in acetone solution. Then, a second layer of PI as encapsulation was spin-coated on top of the device and patterned by oxygen plasma [reactive ion etching (RIE), 40 standard cubic centimeters per minute (sccm), 150 mtorr, 250 W for 10 min] using a photoresist (AZ4620) as a mask. The device fabrication was completed by immersion in buffer oxide etchant (BOE) (6:1; Transene Company Inc.) to release the devices from the glass substrate, and then all were cleaned in deionized (DI) water. The yielded narrow serpentine-shaped open-mesh devices had a total thickness of ~4 μm, as shown in fig. S1 (B and C). The detailed material preparation and device fabrication processes are described in Materials and Methods and are also shown in fig. S2.

The freestanding HMI device, which is placed onto target surfaces, can be handled with media such as a parchment paper and water-soluble tape. Figure S3 illustrates the procedure of using a parchment paper to transfer the device onto a human arm. Figure 1B shows an optical image of a well-adhered HMI device on the forearm. The feats of ultrathin thickness and serpentine-shaped open-mesh geometries render the advantage of seamless and robust adhesion on objects, such as human skin, without the aid of an additional adhesive (9). As shown in Fig. 1C, the thin and narrow serpentine structures form conformal contact with a polymer (Dragon Skin, Smooth-On Inc.) replica of human skin, as examined using a scanning electron microscope (SEM). No obvious delamination was observed even when the skin experienced various modes of deformation, such as compression and stretching (Fig. 1D). To promote and ensure the adhesion durability for long-term wearing or wearing in harsh environments, liquid bandage spray can be applied on top of the ultrathin imperceptible HMI device, which serves as an ultrathin conformal cover once solidified. Figure S4A shows the HMI device on the forearm after liquid bandage spray. The adhesion between the HMI device and skin is not affected (fig. S4B), and the HMI device can survive even underwater rinsing and soap washing (fig. S4C).

To form a closed-loop HMI between a human and the machine, prosthetic skin from such a class of ultrathin stretchable devices was also implemented onto a robotic hand. As one example, the IZO nanomembrane–based temperature sensor array fabricated in the same manner as aforementioned was developed. The prosthetic skin is composed of a thin elastomer of poly(dimethylsiloxane) (PDMS) (~300 μm) and an array of sensors transferred and bonded upon it. The PDMS emulates the stretchability while providing mechanical support, and the arrayed sensors mimic the sensory functions of human skin. Figure 1 (E and F) shows the exploded layer structure of the temperature sensor and an optical image of a prosthetic skin implemented on the robotic hand, respectively. It is noted that the prosthetic skin can endure mechanical deformation such as stretching by ~30% without any delamination, as shown in Fig. 1 (G and H).

Sol-gel-on-polymer–processed IZO nanomembrane and devices

The sol-gel-on-polymer–processed oxide semiconductor is the key to realize multiple functionalities without heterogeneous integration or stitching functional modules. The solution process is promising for scalable manufacturing because it has many advantages such as its simplicity, low cost, uniformity, high throughput, and compositional controllability (20–22). Detailed characterization of the IZO

nanomembrane was performed. Figure S5A shows an SEM image of the patterned IZO nanomembrane on PI. The thickness of the IZO nanomembrane (50 nm) was measured with a profilometer. The sol-gel-on-polymer–processed IZO nanomembrane shows high absorption in the UV region and high transmittance in the visible light region (fig. S5, B and C). The amorphous structure of the IZO nanomembrane was confirmed with x-ray diffraction (XRD) (23), where the 2θ angle with a broad peak only exists near ~33° at low intensity (fig. S5D). The chemical composition was further examined by the O 1s spectrum from x-ray photoelectron spectroscopy (XPS), as shown in fig. S5E. The spectrum was deconvoluted into three fitting curves, with strong peaks centering at ~529.9, 531.3, and 531.9 eV, which correspond to oxygen in the oxide lattice, oxygen vacancy, and oxygen in metal hydroxide, respectively (24, 25). The atomic percentage of oxygen vacancies is 42.45%, which verifies that the IZO nanomembrane is a semiconductor (25, 26).

Data storage devices, such as memory, are indispensable components in wearable HMIs. Although solution-processed materials such as TiO_2 (27), SiO_x (28), and perovskite (29) for memory devices have been reported, they are not readily used for other functionalities as aforementioned. Here, an IZO nanomembrane–based stretchable ReRAM is constructed. Figure 2 (A and B) shows a schematic exploded view of the ReRAM and an optical microscopic image, respectively. The ReRAM was designed with an Au (50 nm)/IZO (50 nm)/Au (50 nm) sandwiched structure with PI encapsulations. The sequential device structures during the fabrication are illustrated by the optical microscopic images in fig. S6A. The detailed device dimensions are shown in fig. S6B. The switching mechanism of the IZO nanomembrane–based ReRAM is attributed to the formation and rupture of conductive filaments of locally concentrated oxygen vacancies (30–32). The vacancies are induced by redox reactions within the IZO layer by an applied electrical voltage along the thickness direction. Under a certain sufficient voltage, oxygen ions and oxygen vacancies are created, and a conductive filament is therefore formed across two electrodes, resulting in a drastic current transition from a high-resistance state (HRS) to a low-resistance state (LRS). Upon applying reverse bias at a certain voltage, the oxygen vacancies initially created become neutralized, causing the conductive filament to rupture and the current to decrease drastically, yielding HRS. Figure S7 schematically illustrates the switching mechanism between LRS and HRS (31, 32). Figure 2C shows the I-V curves of the ReRAM by sweeping the bias voltage, where bistable switching characteristics are presented. The device initially showing HRS drastically switched to LRS at 0.96 V (SET), and the LRS switched back to HRS by applying a negative voltage of −1.6 V (RESET). To evaluate the reliability of the IZO nanomembrane–based ReRAM, we performed write-read-erase-read (WRER) cycles (Fig. 2D) and retention tests. The results show stable operation without obvious degradation during 25 cycles (Fig. 2D and fig. S8A) and continuous sweeping for 2000 s (fig. S8B).

To examine the mechanical strain effect on device performances, we characterized the ReRAM under different levels of mechanical stretching using a custom-made stretcher. The collection of optical images (left frames) of the device and the strain profiles (right frames) of the IZO nanomembrane based on finite-element analysis (FEA) under different mechanical strains is shown in Fig. 2E. The corresponding results of the Au interconnects are shown in fig. S9. These results collectively indicate that the semiconductor experiences minimal and negligible strain when stretched, which reflects the rational design of the device, with the functional components positioned
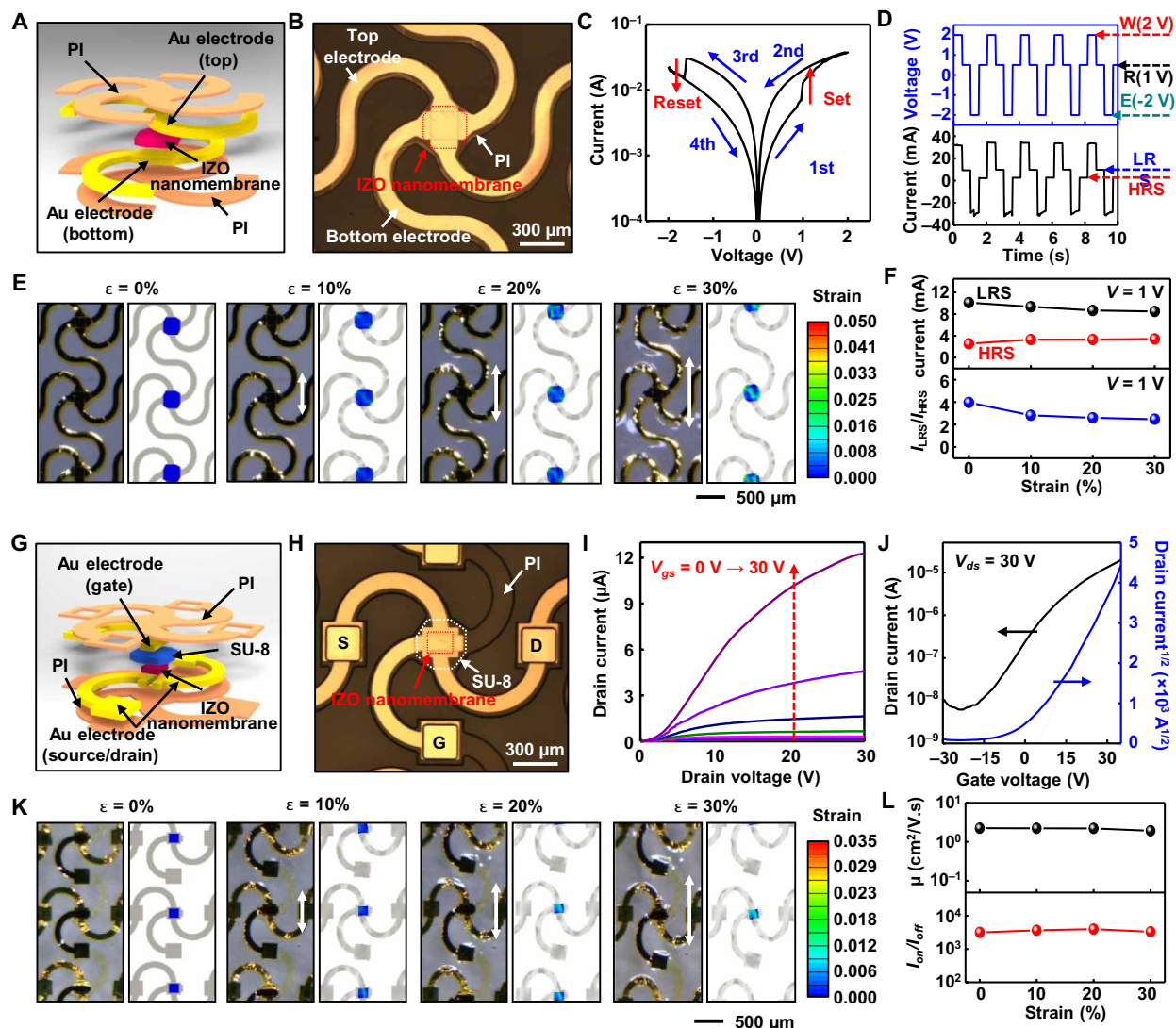
Fig. 2. Characteristics of the ReRAM and FETs. (**A**) Schematic exploded view of the IZO nanomembrane–based ReRAM. (**B**) Optical microscopic image of the ReRAM. (**C**) *I-V* characteristics of the bipolar switching of the ReRAM. (**D**) WRER cycle of the ReRAM. (**E**) Sequential images of the IZO nanomembrane–based ReRAM under strain and corresponding FEA results of IZO. (**F**) Current at LRS and HRS and I_{LRS}/I_{HRS} under strain. (**G**) Schematic exploded view of the IZO FET. (**H**) Optical microscopic image of the FET. (**I**) Output characteristics of the FET. (**J**) Transfer characteristics of the FET. (**K**) Sequential images of the FETs under strain and corresponding FEA results of IZO. (**L**) Calculated field-effect mobility of the IZO and I_{ON}/I_{OFF} of the FET under strain.

near the center of the serpentines to avoid substantial strain. The stretching was accommodated by the serpentine interconnects. Figure 2F shows the electrical current at LRS and HRS as well as I_{LRS}/I_{HRS} under different mechanical strains. In addition, the stable *I-V* characteristics, SET/RESET voltage, and WRER cycles of IZO ReRAM under different mechanical strains are shown in fig. S10. These results indicate that the ReRAM device can function stably under mechanical strain without substantial degradation. It is noted that the IZO ReRAM device performance can be further improved by material and process optimization.

The FET is the fundamental building block for interfacing and switching electronics for HMIs. The top-gate structured FETs were fabricated with the IZO nanomembrane as the channel material and the epoxy (SU-8 2000.5, 500 nm thick, MicroChem) as the gate dielectric, as schematically illustrated in Fig. 2G. Figure 2H shows

the optical image of the FET, and fig. S11A shows sequential optical microscopic images of the device during the fabrication process. The detailed layout and geometries are shown in fig. S11B. The n-type FET output and transfer curves are shown in Fig. 2 (I and J). The transfer curve (in black) was measured with a constant drain voltage of 30 V. The calculated field-effect mobility is 2.24 cm²/V·s. The threshold voltage (V_{th}) is 4.4 V, and the on/off current ratio is about 3.16×10^3. The subthreshold swing is 10.6 V/decade. The details of the calculations are presented in the Supplementary Materials. Dynamic responses of the FET were also characterized based on a load-type inverter by connecting a load resistor with the FET. Alternatively, voltages of −10 and 10 V as square waves (V_{IN}) with different frequencies (100 Hz, 1 kHz, and 10 kHz) were applied, and the output voltage (V_{OUT}) was recorded. Clear dynamic inverting characteristics were obtained (fig. S12). The extracted response time parameters are

summarized in table S1. Similar to the ReRAM, the FETs were positioned in the cross center of the serpentines and experienced negligible mechanical strain when stretched. Figure 2K shows collective optical images (left frames) of the FET and the strain profiles (right frames) of the IZO nanomembrane based on FEA under mechanical strains of 0, 10, 20, and 30%. The strain profiles of the SU-8 gate dielectric and Au electrode under different levels of mechanical stretching are shown in figs. S13 and S14, respectively. Although a slight decrease (from 2.24 to 1.92 cm^2/V·s) of field-effect mobility was observed, the device showed stable operation under mechanical strain up to 30% (Fig. 2L and fig. S15). In addition, cyclic electrical stress by ON/OFF switching for 2000 cycles was applied to the transistor to illustrate the stable and reliable operation (fig. S16). Furthermore, the FETs stored for ~2 years under ambient conditions still show normal operation, which indicates decent environmental stability (fig. S17).

A skin-wearable ultrathin UV sensor is one of the most effective apparatus to monitor UV exposure, which helps to reduce the risk of skin diseases (33, 34). A two-terminal structured UV sensor based on the IZO nanomembrane, working as a UV conductor, was developed by taking advantage of the IZO UV absorption capability and its wide bandgap (~3.18 eV; fig. S5B). The schematic device configuration and optical image are shown in Fig. 3 (A and B, respectively). The device during fabrication is shown in fig. S18A, and the detailed layout is shown in fig. S18 (B and C). The sensor exposes the IZO nanomembrane without PI encapsulation to avoid UV absorption. The photocurrent of the devices under UV illumination is shown in Fig. 3C. The dark current is 1.03×10^{-10} A at a bias of 10 V.
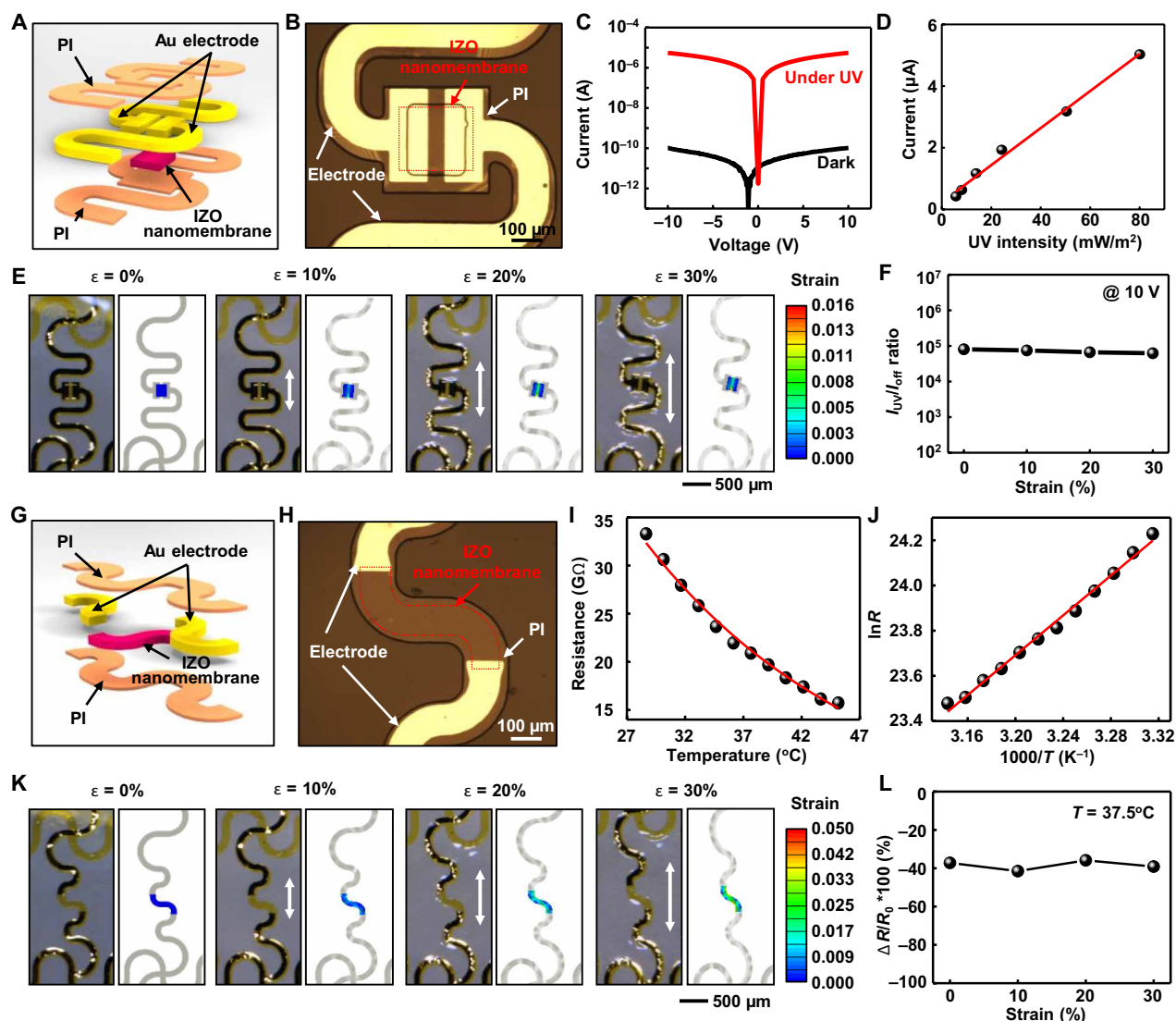

Fig. 3. Characteristics of UV and temperature sensors. (**A**) Schematic exploded view of the IZO nanomembrane–based UV sensor. (**B**) Optical microscopic image of the UV sensor. (**C**) I-V characteristics of the UV sensor. (**D**) Calibration curve of the IZO UV sensor. (**E**) Sequential images of the UV sensor under strain and corresponding FEA results of IZO. (**F**) I_{UV}/I_{dark} for UV light under strain. (**G**) Schematic exploded view of the IZO temperature sensor. (**H**) Optical microscopic image of the temperature sensor. (**I**) Calibration curve of the temperature sensor. (**J**) Plot of ln$R$ versus 1000/T of the temperature sensor. (**K**) Sequential images of the IZO temperature sensor under strain and corresponding FEA results of IZO. (**L**) Relative resistance change of the temperature sensor under strain.

The photocurrent at the UV light intensity of 80.07 mW/m^2 is 5.52×10^{-6} A. The calculated current ratio is 5.35×10^4. The measured photocurrent under different UV light intensities is illustrated in Fig. 3D. The measured I-V curves by sweeping the voltage from −10 to 10 V is shown in fig. S19. The linear characteristics of the I-V curve confirm the working mechanism of a photoconductor. Experiments and FEA studies were performed to investigate the associated strain and sensor performance under mechanical strain. Figure 3E shows collective optical images (left frames) of the FET and the strain profiles (right frames) of the IZO nanomembrane based on FEA under mechanical strains of 0, 10, 20, and 30%. The strain profiles of the Au electrode under different levels of mechanical stretching are shown in fig. S20. Negligible changes of both dark current and photocurrent under different levels of mechanical strain were observed, as shown in fig. S21. These results prove that the devices can be worn and function stably when deformed.

Skin temperature is an important indicator of various health issues (35, 36). A wearable epidermal temperature sensor that can be seamlessly mounted on the skin to precisely and continuously monitor its temperature is a vital device that allows early medical warnings. Owing to its high sensitivity at a low temperature range (−50° to 100°C), the thermistor is a preferred form of temperature sensor for medical applications (37). Here, an ultrathin stretchable thermistor with the IZO nanomembrane as the semiconductor was developed. The schematic two-terminal device configuration and optical image are shown in Fig. 3 (G and H). Figure S22A shows the images of the device before and after the PI encapsulation and patterning. The detailed structure of the device is presented in fig. S22 (B and C). Figure 3I shows the measured resistance at different temperatures between 28.5° and 45.0°C. The normalized resistance change as a function of temperature is shown in fig. S23A. The thermistor's characteristics of a negative temperature coefficient (NTC) are obtained. Figure 3J shows the plot and linear fit of lnR versus the reciprocal of the absolute temperature (1/T), which is fitted by a linear curve. The calculated temperature coefficient (fig. S23B) is comparable to that of a commercially available bulky NTC thermistor (38).

Experiments (left frame) and FEA (right frame) were performed to characterize the sensor upon stretching. Figure 3K shows the experimental optical images (left frames) and the FEA result (right frames) of the IZO semiconducting material in the temperature sensor. The strain distribution of the Au electrode under different mechanical strains is shown in fig. S24. The normalized resistance change shows no substantial change, as shown in Fig. 3L and fig. S25A. The calculated β and α values show stable values under mechanical strain (fig. S25B). These results prove that the IZO temperature sensor operates well under mechanical strain and can be used for wearable sensing devices.

A skin-mountable strain sensor that measures the body's dynamics could provide important information regarding human motion and activities (39, 40). An IZO nanomembrane–based strain sensor that can be used for communication between a human and a robot was developed to further highlight the versatility of this IZO material. The schematic device configuration and optical image are shown in Fig. 4 (A and B). The device during fabrication is shown in fig. S26A, and the detailed layout is shown in fig. S26 (B and C). The strain sensor is designed as a straight narrow ribbon; thus, the strain on the IZO nanomembrane can magnify the overall strain on the device (10, 14, 41). Figure 4C shows the plot of the normalized resistance change as a function of strain from 0 to 30% along the longitudinal direction. The normalized resistance change is mainly attributed to the IZO sensing area rather than the electrode area, because (i) the serpentine structure of Au interconnection can relieve strain and shows negligible resistance (<0.01%) change under a mechanical strain of 30% (fig. S27) and (ii) the resistance of the electrodes is much lower than the IZO sensing element. The calculated gauge factor of the devices is 2.11 ± 0.13 over the strain range of 0 to 30%. The detailed calculation is described in the Supplementary Materials. The measured resistance change during cyclical stretching and releasing at a frequency of 1 Hz under 20% mechanical strain shows a stable and repeatable response (Fig. 4D). Figure 4E presents experimental results (left frames) and the FEA computed strain profile (right frames) of the IZO sensing area under different levels of
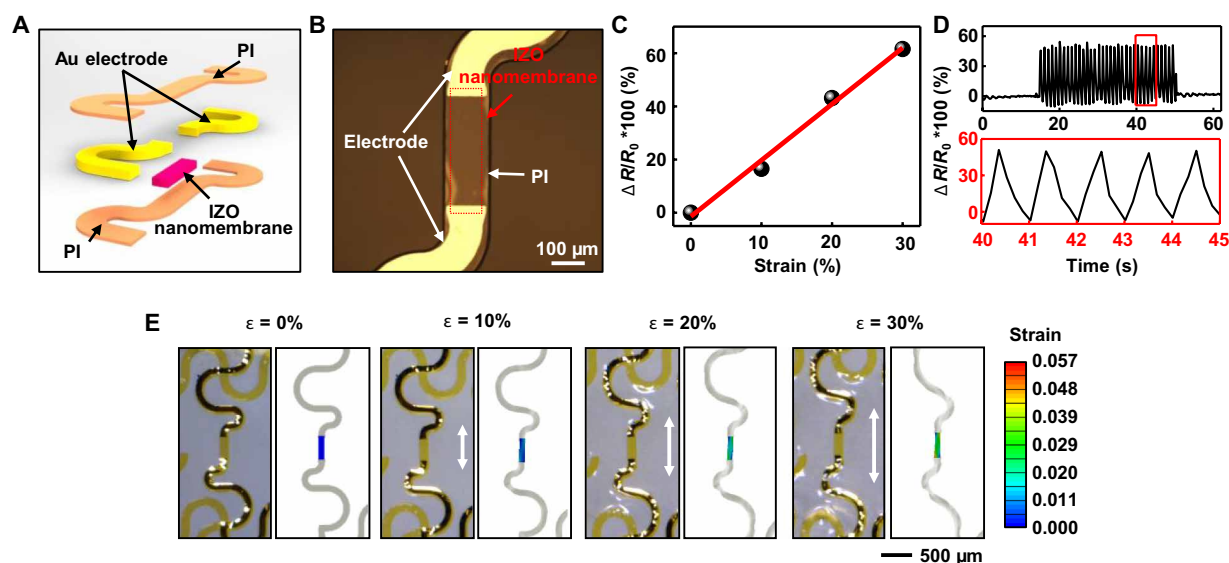

Fig. 4. Characteristics of strain sensor. (**A**) Schematic exploded view of the IZO strain sensor. (**B**) Optical microscopic image of the strain sensor. (**C**) Calibration curve of the strain sensor. (**D**) Relative resistance change of the strain sensor under cyclic stretching and relaxing. (**E**) Sequential images of the strain sensor under strain and corresponding FEA results of IZO.

mechanical stretching. The strain profile of the electrode area based on FEA is shown in fig. S28. The average strain experienced in the gold electrodes and the IZO semiconductor for the strain sensors at different strain rates (30 and 300%/s) was also investigated based on FEA. The strain distribution at different strain rates in the Au electrodes and IZO is shown in fig. S29, and the average strain is summarized in table S2. No substantial difference was found at different strain rates.

Wearable closed-loop HMI system

The demonstrated ultrathin multifunctional IZO nanomembrane–based wearable electronics have substantial advantages such as impercepti-bility, stretchability, and multifunctionality, facilitating the realiza-tion of closed-loop interactive HMIs. The developed interactive HMI system is schematically shown in fig. S30. Wearable sensors on the human skin detect signals such as strain-induced human motion.

The detected signals are then used to control the motion of the ro-botic hand. First, communication between different parts of the hu-man and machine is demonstrated. The IZO strain sensor is placed on the human shoulder to detect strain by the motion of the human arm, as shown in Fig. 5A. The motion of the arm causes a strain change on the shoulder, which was detected by the strain sensor. The strain sensor shows low resistance at the first status, but the resistance increases drastically at the second status due to the mechan-ical strain on the human shoulder, as shown in Fig. 5B. Another important application of HMI is human motion mimicry for usage in hazardous places where people cannot access, such as the scene of a fire or a radioactive contamination zone, or in virtual reality applications where a virtual character can be controlled by sensors on the body. As shown in Fig. 5C, two strain sensors were placed on the back of a human hand with different directions to detect two-dimensional strain from hand motion. No strain detection on either
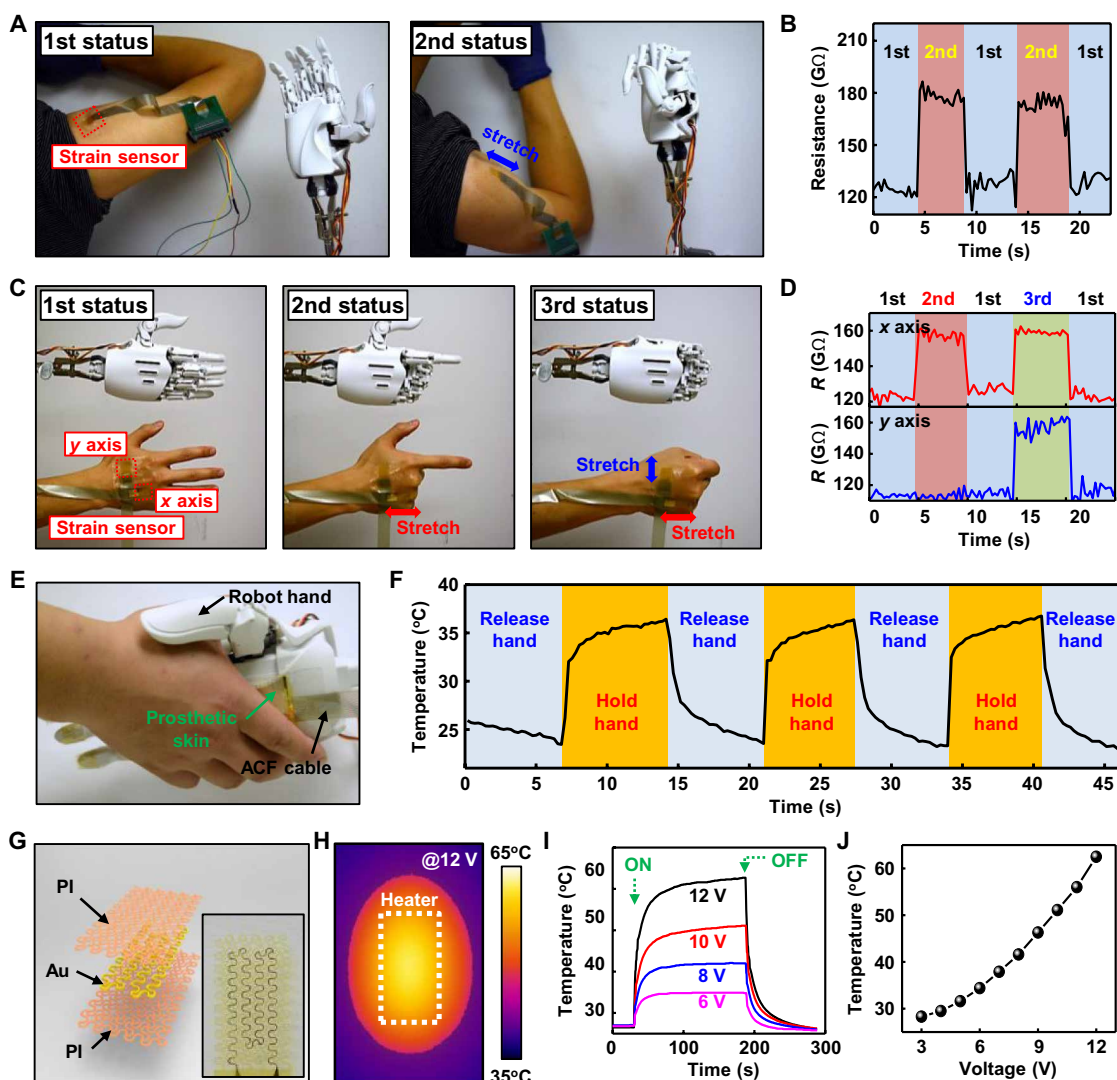
Fig. 5. Wearable closed-loop HMI. (**A**) Representative image of human motion to control the robotic hand. (**B**) Resistance change of strain sensor on the human skin under different human motions. (**C**) Representative image of human motion mimicking. (**D**) Resistance change of strain sensor on human motion mimicking. (**E**) Repre-sentative image of the robotic hand, with the temperature sensor touching the human hand. (**F**) Resistance change of the temperature sensor on the robotic hand while human hand holds the robot. (**G**) Schematic exploded view of the resistive microheater. (**H**) IR temperature mapping of the microheater. (**I**) Dynamic temperature change under different applied voltages. (**J**) Calibration curve of the microheater. Photo credit: Kyoseung Sim, University of Houston.

sensor at the first status causes the robotic hand to maintain its initial shape. When the human hand changes its shape to that of the second status, the x-directional strain sensor detects mechanical strain from the hand motion and induces the change of the robotic hand shape to that of the second status, mimicking the human hand shape. At the third status, the clenched human fist causes strain on both strain sensors, which prompts a change in the robotic hand status again. The measured resistance of both strain sensors is representatively shown in Fig. 5D.

The prosthetic skin based on the IZO temperature sensor on the robotic hand detects the temperature of the external environment or grasped object, which, in turn, determines the appropriate voltage applied to a soft thermal stimulator (i.e., microheater) on the human skin. This microheater generates the appropriate heat that is equivalent to the temperature that the sensor on the robotic hand detected. On the basis of such a series of processes, an interactive closed-loop HMI system can be realized. The sensing properties of the prosthetic skin on the robotic hand were characterized by repeated intervals of holding and releasing the human hand, as shown in Fig. 5E. The measured dynamic temperature response is shown in Fig. 5F. To complete this closed-loop system, an Au-based thermal stimulator is demonstrated and characterized as a stimulating device. Figure 5G shows a schematic drawing and the optical image of the thermal stimulator. The temperature distribution of the thermal stimulator at an applied voltage of 12 V is captured with an infrared (IR) camera (FLIR SC7000; Fig. 5H). The transient temperature upon different applied voltages is shown in Fig. 5I; the temperature first increases and then stabilizes. Figure 5J shows the calibration curve of the stabilized temperature based on the applied voltage. The ultrathin stretchable IZO-based wearable sensor, prosthetic skin, and wearable temperature delivery device together, as one example, enable a closed-loop HMI system.

DISCUSSION

The sol-gel-on-polymer–processed IZO metal oxide nanomembrane exhibits its versatility to be used as ultrathin soft memory devices, transistors, temperature sensors, strain sensors, and UV sensors. The multifunctional devices can be formed simultaneously by one-step solution processing without any heterogeneous integration processes. The ultrathin stretchable and imperceptible electronics-enabled wearable sensors, prosthetic skin, and an actuator device for humans and robotics prove the feasibility of a closed-loop HMI system. Such a type of stretchable device paves the way toward low-cost, scalable manufacturing, wearable HMI devices capable of seamless and robust interfacing with the wearer. In addition, it also enables the wearable HMI device to become a vital technology with enhanced capabilities, comfort, and convenience toward enhanced interaction and teaming between humans and machines.

MATERIALS AND METHODS
Sol-gel-on-polymer IZO nanomembrane preparation
To prepare the IZO nanomembrane (thickness, 50 nm) by the sol-gel-on-polymer process, the precursor was prepared by dissolving zinc acetate dihydrate [$Zn(OAc)_2\cdot2H_2O$, 98.8 mg] and indium(III) nitrate hydrate [$In(NO_3)_3\cdot4H_2O$, 167.8 mg] in 15 ml of 2-methoxyethanol. Then, 300 μl of monoethanolamine was added in the solution. The mixture was stirred for 1 hour, followed by ultrasonication for 2 hours to form a homogeneous solution. All the chemicals were purchased from Sigma-Aldrich and used as received. For the IZO nanomembrane formation, the precursor solution was spin-coated at 2000 rpm for 60 s on a cleaned substrate and prebaked at 100°C on a hot plate for 10 min to remove the organic solvent. The spin-casting process was repeated four times to achieve an appropriate thickness for the active layer. The coated sample was annealed at 300°C on a hot plate for 1 hour.

Characterization of IZO nanomembrane
The thickness of IZO was measured with a surface profilometer (Alpha-Step IQ, KLA-Tencor), and the SEM (XL-30S FEG, Philips) was used to examine the surface morphology. The absorbance and transmittance were characterized by UV-visible spectroscopy (Cary 60 UV-Vis, Agilent Technologies). XRD was performed to investigate the structures of the IZO nanomembrane. The chemical bonding states were characterized by XPS (Physical Electronics model 5700 XPS instrument).

Fabrication of ultrathin multifunctional HMI devices
The fabrication of the ultrathin IZO nanomembrane–based stretchable multifunctional HMI devices began by cleaning a glass substrate with acetone, isopropyl alcohol, and DI water, followed by dehydration at 110°C for 2 min on a hot plate. The PI precursor solution (PI-2545, HD MicroSystems) was spin-coated at 3000 rpm for 30 s on the glass substrate and prebaked at 150°C on a hot plate for 10 min to remove the organic solvent, and then the PI film was fully cured at 250°C on a hot plate under ambient condition for 1 hour. To form electrodes for ReRAMs (bottom electrode), FETs (source and drain electrodes), temperature sensors, UV sensors, and strain sensors and the resistive microheater metal layers (Cr/Au; 3 nm/50 nm) were deposited on the PI by e-beam evaporation and patterned through photolithography and wet chemical etching. Thereafter, the IZO nanomembrane (as the active material) was coated by the abovementioned thin-film formation process, followed by patterning through photolithography and wet etching by a mixture of acetic acid and DI water (50:50, volume %). To form the gate dielectric for FETs, SU-8 (2000.5, MicroChem) was coated and patterned on a desired position by spin casting and photolithography. The top electrode for ReRAM and the gate electrode for FETs were patterned by a liftoff process. A second layer of PI as an encapsulation layer was then formed by spin coating. Last, both the supporting and encapsulation PI layers were patterned using photoresist as a mask by RIE (PlasmaLab 80 Plus, Oxford Instruments) under O_2 environment (40 sccm, 150 mtorr, 250 W) for 10 min.

Preparation for characterization of stretchable devices
The fabricated devices were released from the glass substrate by immersing in BOE (6:1) and rinsed with DI water. To transfer the devices onto a stretchable substrate, our previously reported tape transfer printing was used (*42*). The devices were picked up from the substrate using the tape (3M 3850), followed by deposition of the thin SiO_2 layer (50 nm) by e-beam evaporation. A thin PDMS (1 mm thick, Sylgard 184; the ratio of monomer to cross-linker is 10:1) was prepared for the stretchable substrate and exposed by UV ozone treatment for 5 min to generate hydroxyl terminal groups on PDMS surface. Thereafter, the tape with the device was laminated onto a PDMS substrate and heated at 90°C for 10 min to form strong covalent bonding between the SiO_2 on the device and the PDMS substrate.

To finalize transfer printing, the acetone was applied to the sample, which allows the tape to delaminate from the substrate without leaving residue.

Characterization of IZO nanomembrane–based multiple functional stretchable electronics

The electrical characteristics of the devices were determined with a Keithley 4200-SCS semiconductor analyzer. The electrical characteristics under different mechanical strains were obtained using a customized stretcher. The WRER cycle of the ReRAM was characterized by applying the stepped bias at 2, 1, −2, and 1 V in a repeating manner. The retention test was performed by reading current at a constant bias of 1 V after applying 2 V (SET) and applying −2 V (RESET) for LRS and HRS, respectively. The FET output characteristics were measured by sweeping the drain voltage from 0 to 30 V at stepped gate voltage from 0 to 30 V with a step of 5 V. For transfer characteristics, the device was measured with the gate voltage sweeping from −30 to 30 V at a constant drain voltage of 30 V. For the UV sensor characterization, UV75 Light from Thorlabs was used as the UV light source. The electrical characteristics of the IZO nanomembrane–based temperature sensors were carried out in a dark environment to avoid light effects, with the temperature change measured using the IR and Contact Thermometer (568, Fluke) with a type K thermocouple probe. The strain sensor was tested while it was under different mechanical strains. For the cyclic mechanical stretching and releasing test, an anisotropic conductive film cable (HST-9805-210, Elform) was thermally (200°C for 1 min) bonded to the electrode pad at one side and to the printed circuit board at the other side. The test was performed using an IPC flexural endurance tester (CK-700FET, CKSI Co. Ltd.). For the microheater, by applying a voltage of 12 V, the temperature mapping of the thermal stimulator was captured with an IR camera (FLIR SC7000). The temperature change depending on the applied voltage was characterized using Fluke 566 with a type K thermocouple probe and a DC power supply (GPS-3303, GW Instek).

SUPPLEMENTARY MATERIALS

REFERENCES AND NOTES

1. P. Zhang, *Advanced Industrial Control Technology* (William Andrew, 2010).
2. V. Ravindra, C. Castellini, A comparative analysis of three non-invasive human-machine interfaces for the disabled. *Front. Neurorobot.* **8**, 24 (2014).
3. C. S. L. Tsui, P. Jia, J. Q. Gan, H. Hu, K. Yuan, EMG-based hands-free wheelchair control with EOG attention shift detection, in *2007 IEEE International Conference on Robotics and Biomimetics (ROBIO)*, Sanya, China, 15 to 18 December 2007 (IEEE, 2007), pp. 1266–1271.
4. J.-W. Jeong, W.-H. Yeo, A. Akhtar, J. J. S. Norton, Y.-J. Kwack, S. Li, S.-Y. Jung, Y. Su, W. Lee, J. Xia, H. Cheng, Y. Huang, W.-S. Choi, T. Bretl, J. A. Rogers, Materials and optimized designs for human-machine interfaces via epidermal electronics. *Adv. Mater.* **25**, 6839–6846 (2013).
5. P. F. Pasquina, M. Evangelista, A. J. Carvalho, J. Lockhart, S. Griffin, G. Nanos, P. McKay, M. Hansen, D. Ipsen, J. Vandersea, J. Butkus, M. Miller, I. Murphy, D. Hankin, First-in-man demonstration of a fully implanted myoelectric sensors system to control an advanced electromechanical prosthetic hand. *J. Neurosci. Methods* **244**, 85–93 (2015).
6. S. Lim, D. Son, J. Kim, Y. B. Lee, J.-K. Song, S. Choi, D. J. Lee, J. H. Kim, M. Lee, T. Hyeon, D.-H. Kim, Transparent and stretchable interactive human machine interface based on patterned graphene heterostructures. *Adv. Funct. Mater.* **25**, 375–383 (2015).
7. S. Gong, D. T. H. Lai, Y. Wang, L. W. Yap, K. J. Si, Q. Shi, N. N. Jason, T. Sridhar, H. Uddin, W. Cheng, Tattoolike polyaniline microparticle-doped gold nanowire patches as highly durable wearable sensors. *ACS Appl. Mater. Interfaces* **7**, 19700–19708 (2015).
8. S. Jung, J. H. Kim, J. Kim, S. Choi, J. Lee, I. Park, T. Hyeon, D.-H. Kim, Reverse-micelle-induced porous pressure-sensitive rubber for wearable human–machine interfaces. *Adv. Mater.* **26**, 4825–4830 (2014).
9. N. Lu, C. Lu, S. Yang, J. Rogers, Highly sensitive skin-mountable strain gauges based entirely on elastomers. *Adv. Funct. Mater.* **22**, 4044–4050 (2012).
10. J. Kim, M. Lee, H. J. Shim, R. Ghaffari, H. R. Cho, D. Son, Y. H. Jung, M. Soh, C. Choi, S. Jung, K. Chu, D. Jeon, S.-T. Lee, J. H. Kim, S. H. Choi, T. Hyeon, D.-H. Kim, Stretchable silicon nanoribbon electronics for skin prosthesis. *Nat. Commun.* **5**, 5747 (2014).
11. H. Lee, T. K. Choi, Y. B. Lee, H. R. Cho, R. Ghaffari, L. Wang, H. J. Choi, T. D. Chung, N. Lu, T. Hyeon, S. H. Choi, D.-H. Kim, A graphene-based electrochemical device with thermoresponsive microneedles for diabetes monitoring and therapy. *Nat. Nanotechnol.* **11**, 566–572 (2016).
12. D. Son, J. Lee, S. Qiao, R. Ghaffari, J. Kim, J. E. Lee, C. Song, S. J. Kim, D. J. Lee, S. W. Jun, S. Yang, M. Park, J. Shin, K. Do, M. Lee, K. Kang, C. S. Hwang, N. Lu, T. Hyeon, D.-H. Kim, Multifunctional wearable devices for diagnosis and therapy of movement disorders. *Nat. Nanotechnol.* **9**, 397–404 (2014).
13. D.-H. Kim, J.-H. Ahn, W. M. Choi, H.-S. Kim, T.-H. Kim, J. Song, Y. Y. Huang, Z. Liu, C. Lu, J. A. Rogers, Stretchable and foldable silicon integrated circuits. *Science* **320**, 507–511 (2008).
14. D.-H. Kim, N. Lu, R. Ma, Y.-S. Kim, R.-H. Kim, S. Wang, J. Wu, S. M. Won, H. Tao, A. Islam, K. J. Yu, T.-i. Kim, R. Chowdhury, M. Ying, L. Xu, M. Li, H.-J. Chung, H. Keum, M. McCormick, P. Liu, Y.-W. Zhang, F. G. Omenetto, Y. Huang, T. Coleman, J. A. Rogers, Epidermal electronics. *Science* **333**, 838–843 (2011).
15. T. C. Shyu, P. F. Damasceno, P. M. Dodd, A. Lamoureux, L. Xu, M. Shlian, M. Shtein, S. C. Glotzer, N. A. Kotov, A kirigami approach to engineering elasticity in nanocomposites through patterned defects. *Nat. Mater.* **14**, 785–789 (2015).

16. K. Kalyanam, M. Pachter, M. Patzek, C. Rothwell, S. Darbha, Optimal human–machine teaming for a sequential inspection operation. *IEEE Trans. Hum. Mach. Syst.* **46**, 557–568 (2016).

17. M. Gombolay, A. Bair, C. Huang, J. Shah, Computational design of mixed-initiative human–robot teaming that considers human factors: Situational awareness, workload, and workflow preferences. *Int. J. Rob. Res.* **36**, 597–617 (2017).

18. Y. Lim, S. Ramasamy, A. Gardi, T. Kistan, R. Sabatini, Cognitive human-machine interfaces and interactions for unmanned aircraft. *J. Intell. Robot. Syst.* **91**, 755–774 (2018).

19. M. Pekedis, D. Mascareñas, G. Turan, E. Ercan, C. R. Farrar, H. Yildiz, Structural health monitoring for bolt loosening via a non-invasive vibro-haptics human–machine cooperative interface. *Smart Mater. Struct.* **24**, 085018 (2015).

20. O. Voznyy, B. R. Sutherland, A. H. Ip, D. Zhitomirsky, E. H. Sargent, Engineering charge transport by heterostructuring solution-processed semiconductors. *Nat. Rev. Mater.* **2**, 17026 (2017).

21. Y. S. Rim, H. Chen, X. Kou, H.-S. Duan, H. Zhou, M. Cai, H. J. Kim, Y. Yang, Boost up mobility of solution-processed metal oxide thin-film transistors via confining structure on electron pathways. *Adv. Mater.* **26**, 4273–4278 (2014).

22. Y. S. Rim, H. Chen, Y. Liu, S.-H. Bae, H. J. Kim, Y. Yang, Direct light pattern integration of low-temperature solution-processed all-oxide flexible electronics. *ACS Nano* **8**, 9680–9686 (2014).

23. J. H. Park, S. S. Chae, Y. B. Yoo, J. H. Lee, T. I. Lee, H. K. Baik, Fabrication of solution-processed amorphous indium zinc oxide thin-film transistors at low temperatures using deep-UV irradiation under wet conditions. *Chem. Phys. Lett.* **597**, 121–125 (2014).

24. K. H. Lee, J. H. Park, Y. B. Yoo, W. S. Jang, J. Y. Oh, S. S. Chae, K. J. Moon, J. M. Myoung, H. K. Baik, Effects of solution temperature on solution-processed high-performance metal oxide thin-film transistors. *ACS Appl. Mater. Interfaces* **5**, 2585–2592 (2013).

25. G. Liu, A. Liu, H. Zhu, B. Shin, E. Fortunato, R. Martins, Y. Wang, F. Shan, Low-temperature, nontoxic water-induced metal-oxide thin films and their application in thin-film transistors. *Adv. Funct. Mater.* **25**, 2564–2572 (2015).

26. S. Y. Park, S. Kim, J. Yoo, K.-H. Lim, E. Lee, K. Kim, J. Kim, Y. S. Kim, Aqueous zinc ammine complex for solution-processed ZnO semiconductors in thin film transistors. *RSC Adv.* **4**, 11295–11299 (2014).

27. C. Lee, I. Kim, W. Choi, H. Shin, J. Cho, Resistive switching memory devices composed of binary transition metal oxides using sol–gel chemistry. *Langmuir* **25**, 4274–4278 (2009).

28. J. Yao, J. Lin, Y. Dai, G. Ruan, Z. Yan, L. Li, L. Zhong, D. Natelson, J. M. Tour, Highly transparent nonvolatile resistive memory devices from silicon oxide and graphene. *Nat. Commun.* **3**, 1101 (2012).

29. J. S. Han, Q. V. Le, J. Choi, K. Hong, C. W. Moon, T. L. Kim, H. Kim, S. Y. Kim, H. W. Jang, Air-stable cesium lead iodide perovskite for ultra-low operating voltage resistive switching. *Adv. Funct. Mater.* **28**, 1705783 (2018).

30. S. Kim, S. Choi, W. Lu, Comprehensive physical model of dynamic resistive switching in an oxide memristor. *ACS Nano* **8**, 2369–2376 (2014).

31. M.-C. Chen, T.-C. Chang, C.-T. Tsai, S.-Y. Huang, S.-C. Chen, C.-W. Hu, S. M. Sze, M.-J. Tsai, Influence of electrode material on the resistive memory switching property of indium gallium zinc oxide thin films. *Appl. Phys. Lett.* **96**, 262110 (2010).

32. Y. Yang, W. Lu, Nanoscale resistive switching devices: Mechanisms and modeling. *Nanoscale* **5**, 10076–10092 (2013).

33. H. Araki, J. Kim, S. Zhang, A. Banks, K. E. Crawford, X. Sheng, P. Gutruf, Y. Shi, R. M. Pielak, J. A. Rogers, Materials and device designs for an epidermal UV colorimetric dosimeter with near field communication capabilities. *Adv. Funct. Mater.* **27**, 1604465 (2017).

34. Y. Shi, M. Manco, D. Moyal, G. Huppert, H. Araki, A. Banks, H. Joshi, R. McKenzie, A. Seewald, G. Griffin, E. Sen-Gupta, D. Wright, P. Bastien, F. Valceschini, S. Seité, J. A. Wright, R. Ghaffari, J. Rogers, G. Balooch, R. M. Pielak, Soft, stretchable, epidermal sensor with integrated electronics and photochemistry for measuring personal UV exposures. *PLOS ONE* **13**, e0190233 (2018).

35. K. Takei, W. Honda, S. Harada, T. Arie, S. Akita, Toward flexible and wearable human-interactive health-monitoring devices. *Adv. Healthc. Mater.* **4**, 487–500 (2015).

36. Y. Chen, B. Lu, Y. Chen, X. Feng, Breathable and stretchable temperature sensors inspired by skin. *Sci. Rep.* **5**, 11505 (2015).

37. J. P. Bentley, Temperature sensor characteristics and measurement system design. *J. Phys. E* **17**, 430–439 (1984).

38. F. C. S. Luz, S. A. Pianaro, C. E. Yurk, G. Capobianco, A. J. Zara, S. M. Tebcherani, Construction and testing of a system for the electrical characterization of ceramic thermistors at low temperatures. *Cerâmica* **60**, 96–101 (2014).

39. M. Amjadi, A. Pichitpajongkit, S. Lee, S. Ryu, I. Park, Highly stretchable and sensitive strain sensor based on silver nanowire–elastomer nanocomposite. *ACS Nano* **8**, 5154–5163 (2014).

40. K. K. Kim, S. Hong, H. M. Cho, J. Lee, Y. D. Suh, J. Ham, S. H. Ko, Highly sensitive and stretchable multidimensional strain sensor with prestrained anisotropic metal nanowire percolation networks. *Nano Lett.* **15**, 5240–5247 (2015).

41. D.-H. Kim, R. Ghaffari, N. Lu, S. Wang, S. P. Lee, H. Keum, R. D'Angelo, L. Klinker, Y. Su, C. Lu, Y.-S. Kim, A. Ameen, Y. Li, Y. Zhang, B. de Graff, Y.-Y. Hsu, Z. Liu, J. Ruskin, L. Xu, C. Lu, F. G. Omenetto, Y. Huang, M. Mansour, M. J. Slepian, J. A. Rogers, Electronic sensor and actuator webs for large-area complex geometry cardiac mapping and therapy. *Proc. Natl. Acad. Sci. U.S.A.* **109**, 19910–19915 (2012).

42. K. Sim, S. Chen, Y. Li, M. Kammoun, Y. Peng, M. Xu, Y. Gao, J. Song, Y. Zhang, H. Ardebili, C. Yu, High fidelity tape transfer printing based on chemically induced adhesive strength modulation. *Sci. Rep.* **5**, 16133 (2015).

43. G. Yoo, H. Park, M. Kim, W. G. Song, S. Jeong, M. H. Kim, H. Lee, S. W. Lee, Y. K. Hong, M. G. Lee, S. Lee, S. Kim, Real-time electrical detection of epidermal skin MoS$_2$ biosensor for point-of-care diagnostics. *Nano Res.* **10**, 767–775 (2017).

44. Y. Khan, M. Garg, Q. Gui, M. Schadt, A. Gaikwad, D. Han, N. A. D. Yamamoto, P. Hart, R. Welte, W. Wilson, Flexible hybrid electronics: Direct interfacing of soft and hard electronics for wearable health monitoring. *Adv. Funct. Mater.* **26**, 8764–8775 (2016).

45. S. Sahoo, S. K. S. Parashar, S. M. Ali, CaTiO$_3$ nano ceramic for NTCR thermistor based sensor application. *J. Adv. Ceram.* **3**, 117–124 (2014).

46. S. Jagtap, S. Rane, U. Mulik, D. Amalnerkar, Thick film NTC thermistor for wide range of temperature sensing. *Microelectron. Int.* **24**, 7–13 (2007).

Science Advances

Metal oxide semiconductor nanomembrane–based soft unnoticeable multifunctional electronics for wearable human-machine interfaces

Kyoseung Sim, Zhoulyu Rao, Zhanan Zou, Faheem Ershad, Jianming Lei, Anish Thukral, Jie Chen, Qing-An Huang, Jianliang Xiao and Cunjiang Yu

ARTICLE TOOLS	http://advances.sciencemag.org/content/5/8/eaav9653
SUPPLEMENTARY MATERIALS	http://advances.sciencemag.org/content/suppl/2019/07/29/5.8.eaav9653.DC1
REFERENCES	This article cites 44 articles, 3 of which you can access for free http://advances.sciencemag.org/content/5/8/eaav9653#BIBL
PERMISSIONS	http://www.sciencemag.org/help/reprints-and-permissions

Use of this article is subject to the Terms of Service